Multiple Sclerosis: Validation of MR Imaging for Quantification and Detection of Iron[1]

Andrew J. Walsh, BSc
R. Marc Lebel, PhD
Amir Eissa, PhD
Gregg Blevins, MD
Ingrid Catz, MSc
Jian-Qiang Lu, MD
Lothar Resch, MD
Edward S. Johnson, MD
Derek J. Emery, MD
Kenneth G. Warren, MD
Alan H. Wilman, PhD

Purpose: To investigate the relationship between iron staining and magnetic resonance (MR) imaging measurements in postmortem subjects with multiple sclerosis (MS).

Materials and Methods: Institutional ethical approval was obtained, and informed consent was obtained from the subjects and/or their families. Four MR imaging methods based on transverse relaxation (T2 weighting, R2 mapping, and R2* mapping) and phase imaging were performed by using a 4.7-T system in three in situ postmortem patients with MS less than 28 hours after death and in one in vivo patient 1 year before death. Iron staining with the Perls iron reaction was performed after brain extraction. Region-of-interest measurements from six subcortical gray matter structures were obtained from MR imaging and then correlated with corresponding locations on photographs of iron-stained pathologic slices by using a separate linear least-squares regression in each subject. Iron status of white matter lesions, as determined by staining, was compared with appearance on MR images.

Results: R2* mapping had the highest intrasubject correlations with iron in subcortical gray matter (R^2 = 0.857, 0.628, and 0.685; all $P < .001$), while R2 mapping (R^2 = 0.807, 0.615, 0.628, and 0.489; $P < .001$ and $P = .001$, .034, and .001, respectively), phase imaging (R^2 = 0.672, 0.441, 0.596, 0.548; all $P \leq .001$), and T2-weighted imaging (R^2 = 0.463, 0.582, 0.650, and 0.551; all $P < .001$) had lower but still strong correlations. Within lesions, hypointense areas on phase images did not always represent iron. A hyperintense rim surrounding lesions on R2* maps was only present with iron staining, yet not all iron-staining lesions had R2* rim hyperintensity.

Conclusion: All four MR imaging methods had significant linear correlations with iron and could potentially be used to determine iron status of subcortical gray matter structures in MS, with R2* mapping being preferred. A reliable method of determining iron status within MS lesions was not established.

[1] From the Department of Biomedical Engineering (A.J.W., R.M.L., A.E., A.H.W.), Division of Neurology (G.B., I.C., K.G.W.), Department of Laboratory Medicine and Pathology (J.Q.L., L.R., E.S.J.), and Department of Radiology and Diagnostic Imaging (D.J.E.), University of Alberta, 1098 RTF, Edmonton, AB, Canada T6G 2V2. Received April 17, 2012; revision requested June 1; revision received July 29; accepted August 20; final version accepted September 5. Supported by Natural Sciences and Engineering Research Council of Canada, Canadian Institutes of Health Research, and Multiple Sclerosis Society of Canada. A.J.W. supported by a Vanier Canada Graduate Scholarship and an Alberta Innovates Health Solutions MD/PhD studentship. **Address correspondence to** A.H.W. (e-mail: *alan.wilman@ualberta.ca*).

Iron has an important physiologic role in the brain, including involvement in myelin synthesis, neurotransmitter production, and oxygen transport (1). In multiple sclerosis (MS), iron is reportedly increased in subcortical gray matter and present in some lesions at histologic analysis (2–4). Magnetic resonance (MR) imaging offers a number of methods that are sensitive to brain iron, including T2-weighted fast spin-echo (SE) imaging (5), T2*-weighted gradient-echo imaging (6), mapping of the SE and gradient-echo transverse relaxation rates (R2 and R2*, respectively) (7), phase imaging (8), and susceptibility mapping (9). These methods provide enhanced iron sensitivity at higher magnetic field strengths (7,10). Several MR imaging methods have shown a relationship between subcortical gray matter measures and functional scores in patients with MS (11–13); however, the contribution from iron to the quantitative MR imaging measures is unclear, and image contrast could be derived from other sources, such as macromolecules (14) and protein and lipid orientation (15). Researchers in many studies (14,16–18) have examined the relationship between quantitative MR imaging measurements and predicted brain iron content determined from referenced healthy brain iron values, typically by using the 1958 work of Hallgren and Sourander (19); however, no reference exists for brains with pathologic changes. Postmortem studies are required to determine the relationship between MR imaging measures and actual iron levels in patients with MS.

Few postmortem studies have evaluated the accuracy of quantitative MR imaging methods for measuring brain iron in healthy individuals or in patients with other non-MS diseases. The results of these studies demonstrate that phase (20) and R2 and R2* (21) have a high correlation to iron in these subjects. However, these results cannot be directly translated into evaluating iron in patients with MS because each MR imaging method is variably influenced by different pathologic processes, such as demyelination, cellular infiltration, and edema. Furthermore, most postmortem MR imaging studies that have investigated the relationship between MR imaging and iron have used formalin-fixed tissue (20,22–24). Formalin fixation can alter relaxation properties and, to a lesser extent, the iron content of tissue (25–29). Early in situ postmortem imaging closely resembles in vivo imaging because the brain is surrounded by cerebrospinal fluid, and air-tissue interfaces are intact to cause susceptibility effects that are an important feature in R2* mapping and phase imaging.

In our study, four iron-sensitive methods were evaluated for brain iron detection in patients with MS. In vivo and in situ postmortem MR imaging was followed by Perls iron staining, which enables correlation analysis between MR imaging and iron staining measures in subcortical gray matter and MR imaging detection of iron presence within lesions. Since the imaging parameters are suitable for in vivo acquisition, postmortem results are directly translatable to in vivo human applications. Therefore, the purpose of our work was to investigate the postmortem relationship between iron staining and MR imaging measurements in subjects with MS.

Advances in Knowledge

- Transverse relaxation and phase measures have significant correlation to iron staining in subcortical gray matter of patients with multiple sclerosis (MS).
- R2* mapping has a higher correlation (R^2 = 0.857, 0.628, 0.685; all $P < .001$) to iron in subcortical gray matter structures in MS compared with R2 mapping (R^2 = 0.807, 0.615, 0.628, 0.489; all $P \leq .034$), phase imaging (R^2 = 0.672, 0.441, 0.596, 0.548; all $P \leq .001$), and T2-weighted imaging (R^2 = 0.463, 0.582, 0.650, 0.511; all $P < .001$).
- Hypointense MS lesions on phase images do not always contain iron and can result from demyelination.
- Hyperintense rims around MS lesions on R2* maps were only present in iron-staining lesions.

Implication for Patient Care

- In subcortical gray matter in MS, hypointensity with T2-weighting, increases in transverse relaxation rate, and more negative phase can mainly be attributed to iron.

Materials and Methods

Subjects

Four deceased subjects with MS were included in our prospective study between April 1, 2009, and September 13, 2011. Institutional ethical approval was obtained, as was informed consent from the subjects and/or their families. Three subjects with secondary progressive MS underwent postmortem in situ MR imaging shortly after death. Subject 1 was a 63-year-old man who had longstanding type 2 diabetes with neuropathologic evidence of hyalinized vessels, which is consistent with this disease. This subject died of cardiorespiratory failure due to a combination of aspiration pneumonia and septicemia from pyelonephritis and was imaged 28 hours after death. Subject 2 was a 55-year-old woman who had a history of chronic obstructive pulmonary disease and generalized anxiety

Published online before print
10.1148/radiol.12120863 **Content code:** NR

Radiology 2013; 267:531–542

Abbreviations:
MS = multiple sclerosis
ROI = region of interest
SE = spin echo

Author contributions:
Guarantors of integrity of entire study, A.J.W., G.B., A.H.W.; study concepts/study design or data acquisition or data analysis/interpretation, all authors; manuscript drafting or manuscript revision for important intellectual content, all authors; approval of final version of submitted manuscript, all authors; literature research, A.J.W., G.B., J.Q.L.; clinical studies, A.J.W., G.B., I.C., J.Q.L., D.J.E., K.G.W.; experimental studies, A.J.W., R.M.L., A.E., L.R., E.S.J., D.J.E., A.H.W.; statistical analysis, A.J.W.; and manuscript editing, A.J.W., R.M.L., G.B., I.C., J.Q.L., L.R., E.S.J., D.J.E., A.H.W.

Conflicts of interest are listed at the end of this article.

disorder. This subject died of aspiration pneumonia and was imaged 6 hours after death. Subject 3 was a 60-year-old man who had longstanding chronic obstructive pulmonary disease, longstanding congestive heart failure, and metastatic prostate cancer. This subject died of *Staphylococcus aureus* septicemia due to pneumonia secondary to prostate cancer lung metastasis and was imaged 7 hours after death. Subject 4 had relapsing-remitting MS with no other longstanding medical conditions. This subject underwent in vivo imaging 1 year before death at the age of 45 years and died of medullary compression due to a B-cell lymphoma tumor in the cerebellum. In all subjects, the clinical diagnosis of MS was made by neurologists who specialize in MS (K.G.W. and G.B., with 38 and 6 years experience, respectively) and was pathologically confirmed by three neuropathologists (E.S.J., J.Q.L., and L.R., with 34, 5, and 30 years experience, respectively).

MR Image Acquisition

MR imaging data were acquired by using a 4.7-T whole-body imaging system (Varian Unity Inova, Palo Alto, Calif). The imaging protocol consisted of four axial MR imaging methods that took a total time of 39 minutes: standard T2-weighted fast SE (6.8 minutes) (30), R2* mapping (8.9 minutes), R2 mapping (15.6 minutes) (31), and phase imaging (6.6 minutes). Subject 2 did not undergo imaging with the R2* mapping sequence.

Axial two-dimensional T2-weighted fast SE MR imaging was acquired with 80-mm superior-inferior coverage centered on the thalamus with slightly different parameters between subjects. Typical parameters were: repetition time msec/echo time msec, 7000–14000/30–50; echo train length, four to eight; 40–80 contiguous sections; section thickness, 1–2 mm; field of view, 256 × 192.5 mm; matrix, 1024 × 385 with 75% partial Fourier; voxel size, 0.25 × 0.25 × 1–2 mm. This echo time provided substantial T2-weighting for iron-containing deep gray matter at 4.7 T (12).

Axial three-dimensional R2* mapping was acquired with full brain coverage (160 mm) by using the following parameters: repetition time, 44 msec; 10 echoes with 4.0–4.2 msec echo spacing; first echo, 2.9–3.2 msec; flip angle, 11°; field of view, 256 × 128–160 × 160 mm; matrix, 512 × 160 × 80; voxel size, 1 × 0.8–1 × 2 mm.

Axial two-dimensional R2 mapping with a multiecho SE was acquired by using the following parameters: repetition time, 3500 msec; 18–24 echoes with 10-msec echo spacing; first echo, 10 msec; two sections, section thickness, 4–5 mm; section gap, 8–10 mm, field of view, 256 × 181 mm; matrix, 512 × 145–171; voxel size, 0.8–1 × 1 × 4–5 mm. The section thickness of the 180° refocusing pulses was 1.75 times wider than that of the excitation pulse. In vivo specific absorption rate standards allowed only two sections of R2 mapping to be collected over a 5.2-minute acquisition owing to the high magnetic field and the large number of 180° pulses. The sequence was implemented multiple times to acquire data between interleaved sections. Three acquisitions were performed in subjects 1 and 4, two were performed in subject 2, and one was performed in subject 3.

Axial phase imaging used a two-dimensional single gradient echo with first-order flow compensation acquired with the following parameters: 1540/7–15; 50 contiguous sections; section thickness, 2 mm; flip angle, 70°; field of view, 214–256 × 163–192 mm; matrix, 512 × 256–392; voxel size, 0.42–0.5 × 0.42–0.5 × 2 mm.

Images were acquired with a standard birdcage head coil for transmission and a tight-fitting four-element array coil for signal reception. In subject 1, the head coil was also used for reception owing to large head size.

Pathology Examination

The brains were fixed in 18% formalin, sectioned into 8-mm slices, and photographed before iron staining. Coronal cuts were used based on neuropathology preference, except in subject 1, in whom slices were cut axially. Slices containing subcortical gray matter and/or lesions were stained by using the Perls iron reaction (32). The slices were placed in a plastic container with 1 L of 2% hydrochloric acid combined with 1 L of 2% potassium ferrocyanide for 30 minutes. After washing for 2 minutes with water, the slices were photographed again.

The photographs were converted to grayscale by using software (ImageJ [33]) and manually rotated, resized, and translated to align the photographs of stained and unstained brain slices. The window and level were normalized on the basis of the intensity of the static background outside of the brain and the intensity of white matter with little staining within the brain slice. Regions of interest (ROIs) were drawn around iron-rich subcortical gray matter structures, and the differences between structures on stained versus unstained photographs were calculated. The results were divided by the difference between the background and the healthy-appearing white matter, generating a relative optical density where a higher optical density corresponds relatively to more iron staining within one subject. This method is similar to that used in a previous quantitative iron validation study (34) with MR imaging using optical density measures. Lesions were visually examined for iron staining and confirmed as MS lesions with microscopic examination by pathologists (E.S.J. and J.Q.L.) with 100% interobserver reliability.

MR Image Processing

All MR images were interpolated to isotropic 0.25-mm resolution and manually registered, on the basis of gyri contours and subcortical gray matter structures, to the pathologic photographs by using affine transformations. With software (ImageJ), ROIs were drawn around the borders of corresponding subcortical gray matter structures after registration with the pathologic photographs to obtain proper anatomic correspondence. This enabled an accurate spatial comparison of the reformatted axial MR images to the coronal gross pathologic slices for subjects 2, 3, and 4. ROIs were based on the T2-weighted

fast SE MR images and the R2* maps and then transferred to the other images. The structures evaluated included the caudate nucleus, putamen, globus pallidus, substantia nigra, red nucleus, thalamus, and subthalamic nucleus.

Large spatial signal intensity variations on the T2-weighted fast SE MR images, arising from high-field-strength radiofrequency transmittance interference effects (35) and receiver coil variation, were corrected by using a three-dimensional Gaussian blur with a radius of 64 mm. Measured values were divided by the intensity of cerebrospinal fluid averaged between the right and left lateral ventricles.

R2* maps were produced by using a weighted least-squares monoexponential fit of the 10 echoes (36). Prior to fitting, a linear field-gradient correction algorithm was applied to recover signal losses from air-tissue interfaces that were in close proximity to relevant subcortical gray matter structures (37). Weighting factors for the least-squares fitting were given by the intensity scaling factors needed to compensate for signal loss and accounted for amplified noise during the fitting procedure.

R2 maps were produced by using a least-squares fit with stimulated echo compensation (31), which accounted for the exact signal decay that arose from radiofrequency transmittance variation across the section profile and in-plane variation from high-field-strength radiofrequency interference effects.

Phase images were processed with the standard Hanning filter method (38) by using a filter width of 0.125. The filter width is the ratio of the Hanning filter divided by the total matrix size along one dimension (39,40). The phase images were separately processed with a moving window gradient fitting method (40) with a filter width of 0.0625. To mitigate effects of nonlocal external field effects from iron-rich structures, reference phase measures were obtained in nearby healthy-appearing white matter greater than 10 mm from each structure and separately obtained directly adjacent to each structure (40).

MR Imaging Lesion Evaluation

MR imaging lesion contrast was compared between iron-staining and non–iron-staining lesions by a neuroradiologist (D.J.E., with 15 years experience) and a neuropathologist (E.S.J.). Intensity was examined both within lesions and around the periphery (rim) by using phase images, R2* maps, and T2-weighted fast SE MR images. R2 mapping was not used owing to limited coverage. Lesions in subject 4 were not evaluated because of potential variability in lesion activity over 1 year.

Statistical Analysis

Statistical analysis was performed by using software (SPSS, version 18.0 for Macintosh; IBM, Armonk, NY). Correlations between iron-staining optical densities and individual MR imaging measures were tested by using a separate linear regression model in each subject. More than one measurement from a single structure was sometimes obtained owing to the number of slices through that structure at pathologic sectioning. *P* values less than .05 were considered to indicate a significant difference.

Results

Subcortical Gray Matter Measurements

All MR imaging measures showed a significant correlation to iron detected with Perls iron staining (Table 1; Figs 1, 2). R2* measurements had the strongest correlations to optical density in each subject (R^2 = 0.857, 0.628, and 0.685; all $P < .001$). R2 mapping (R^2 = 0.807, 0.615, 0.628, and 0.489; $P < .001$ and $P = .001$, .034, and .001, respectively), phase imaging (R^2 = 0.672, 0.441, 0.596, and 0.548; all $P \leq .001$), and T2-weighted fast SE MR imaging (R^2 = 0.463, 0.582, 0.650, and 0.511; all $P < .001$) had comparable correlations to optical density. A somewhat weaker correlation was evident between the T2-weighted fast SE MR measures and iron in subject 4 (Table 1, Fig 2) while the other MR imaging measures had substantially higher correlations to postmortem staining. Although most subcortical gray matter structures were imaged with the R2 mapping sequence, this regression contained fewer ROIs because the exact anatomic correspondence to pathologic slices was not achieved in all regions owing to section gaps in some subjects.

The phase analysis methods demonstrated different correlations to iron staining (Table 2) and depended strongly on the location of the reference phase measurements. The gradient fitting background removal method with an adjacent reference phase demonstrated the highest correlation to optical density and was the only phase method which demonstrated significant results for all subjects.

Visual Analysis of Subcortical Gray Matter

Hyperintense regions on the R2* and R2 maps and hypointense regions on T2-weighted fast SE MR images corresponded well to staining of subcortical gray matter with Perls iron stain on photographs (Fig 3a, 3b). Postmortem MR imaging depicted similar contrast to in vivo results (Fig 4).

The gradient phase removal method produced more contrast in large subcortical gray matter structures, such as the head of the caudate nucleus, putamen, and globus pallidus, compared with the Hanning processing method (Fig 3c). The Hanning method does not completely remove phase wraps from structures of interest, eliminating quantitative measures in these regions. Within structures, there is some disparity compared with staining and other MR imaging methods with both Hanning and gradient phase methods (Fig 3).

Visual Analysis of MS Lesions

When using T2-weighted fast SE MR images, phase images, and R2* maps, general trends appear when classifying lesions on the basis of iron staining (Table 3). However, convincing evidence for the ability of individual MR imaging methods to be used to determine the iron status of lesions was not established.

Table 1

Correlations between Quantitative MR Imaging Measures and Optical Densities

	R2* Map		R2 Map		T2-weighted Fast SE MR Imaging		Phase MR Imaging		No. of ROIs	
Subject	R^2	*P* Value	R^2	*P* Value	R^2	*P* Value	R^2	*P* Value	R2*, T2-weighted Fast SE, and Phase	R2
1	0.685	<.001	0.489	.001	0.511	<.001	0.548	<.001	22	18
2	ND	ND	0.628	.034	0.650	<.001	0.596	.001	15	7
3	0.628	<.001	0.615	.001	0.582	<.001	0.441	<.001	27	15
4*	0.857	<.001	0.807	<.001	0.463	<.001	0.672	<.001	32	27

Note.—ND = no data.

* In vivo MR imaging.

Figure 1

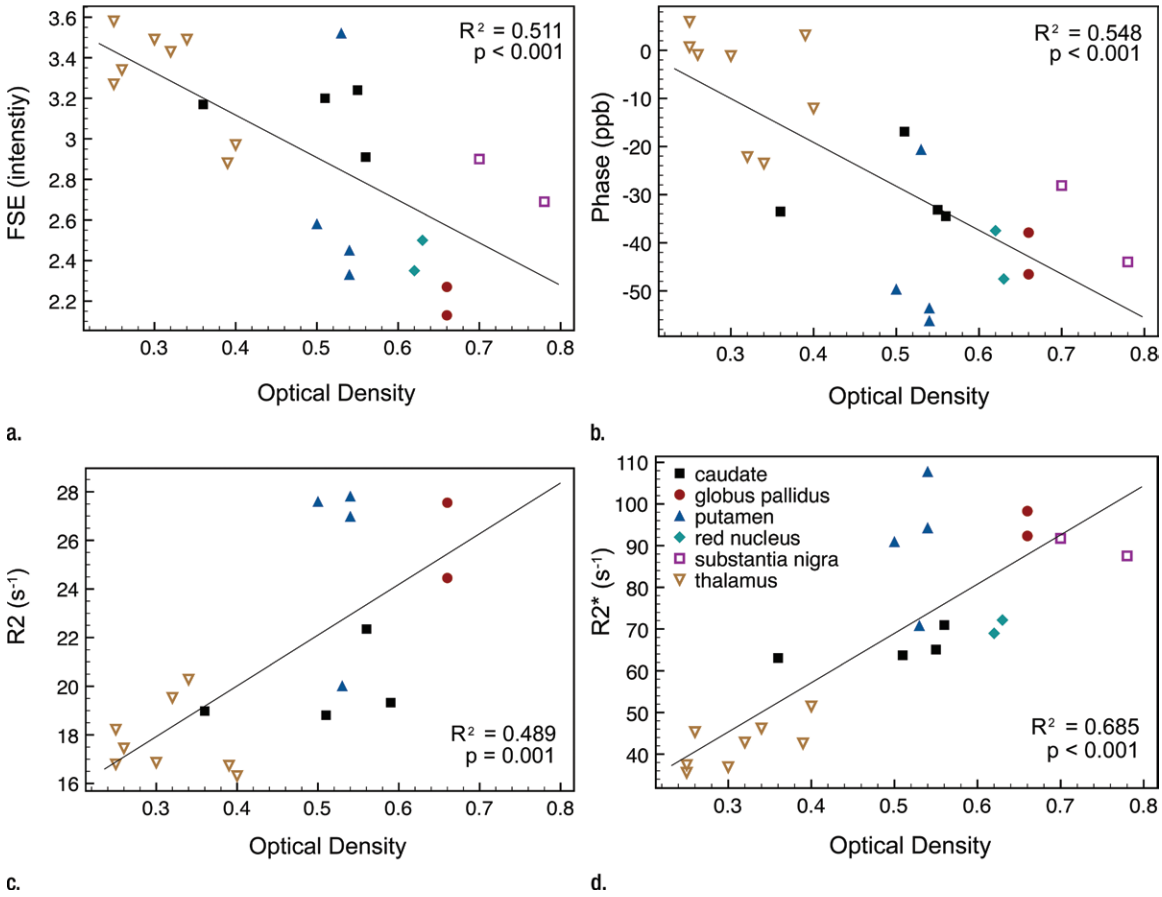

Figure 1: Scatterplots show correlations between optical density from iron staining and in situ postmortem **(a)** fast SE *(FSE)*, **(b)** phase, **(c)** R2, and **(d)** R2* MR imaging in subject 1. Key for all plots appears on **d**. *Caudate* = caudate nucleus, *ppb* = parts per billion, *s* = seconds.

Sixteen lesions, both staining and nonstaining, were seen on pathologic samples from subject 1 (Fig 5). Three lesions could not be analyzed because of partial volume effects on MR images from the lateral ventricles. On R2* maps, hyperintense rims were only present in iron-staining lesions, while on phase images, hypointense rims were generally, but not exclusively, present in iron-staining lesions. Generally, lesions that stained for iron were

Table 2

Correlations between Phase MR Imaging and Optical Densities

	Hanning Standard Filtering				Gradient Fitting					
	White Matter Reference		Adjacent Reference		White Matter Reference		Adjacent Reference		No. of ROIs	
Subject	R^2	*P* Value	R^2	*P* Value	R^2	*P* Value	R^2	*P* Value	Standard Filtering	Gradient Fitting
1	0.217	.069	0.507	.002	0.012	.626	0.548	<.001	16	22
2	0.287	.040	0.255	.114	0.142	.167	0.596	.001	15	15
3	0.059	.233	<0.001	.973	0.011	.609	0.441	<.001	27	27
4*	0.212	.008	0.118	.056	0.004	.738	0.672	<.001	32	32

Note.—White matter reference = healthy-appearing white matter at least 10 mm from the structure border, lateral to all structures. Adjacent reference = white matter directly adjacent to the structural border, medial to the globus pallidus and lateral to all other structures.

* In vivo MR imaging.

Figure 2

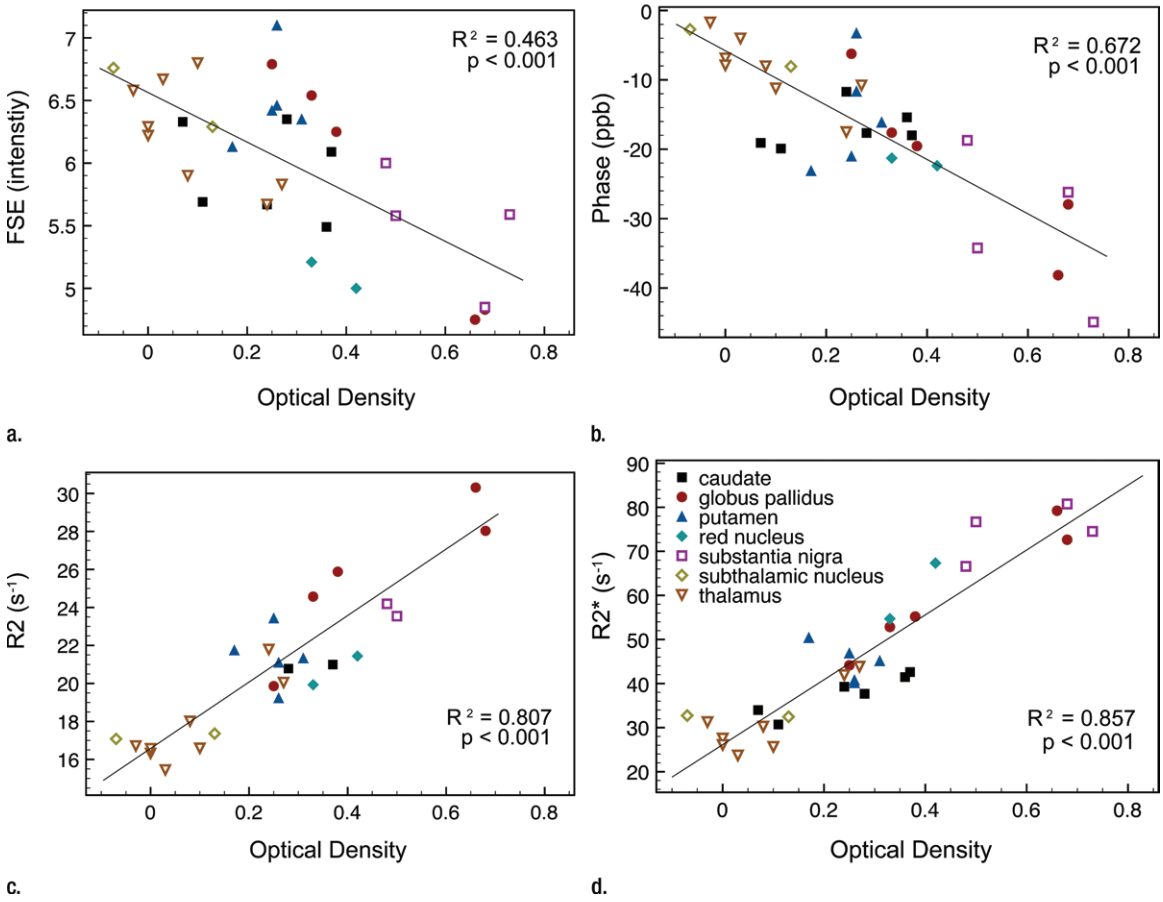

Figure 2: Scatterplots show correlation between optical density from iron staining and in vivo **(a)** fast SE *(FSE)*, **(b)** phase, **(c)** R2, and **(d)** R2* MR imaging in subject 4. Iron staining was performed 1 year after MR imaging, immediately following death. Key for all plots appears on **d**. *Caudate* = caudate nucleus, *ppb* = parts per billion, *s* = seconds.

centrally isointense or not as hypointense on R2* maps as compared with lesions that did not stain. Also, iron-staining lesions often appeared more hypointense centrally on phase images compared with nonstaining lesions; however, some hypointense lesions did not contain iron. All lesions in this subject were hyperintense on T2-weighted fast SE MR images.

Figure 3

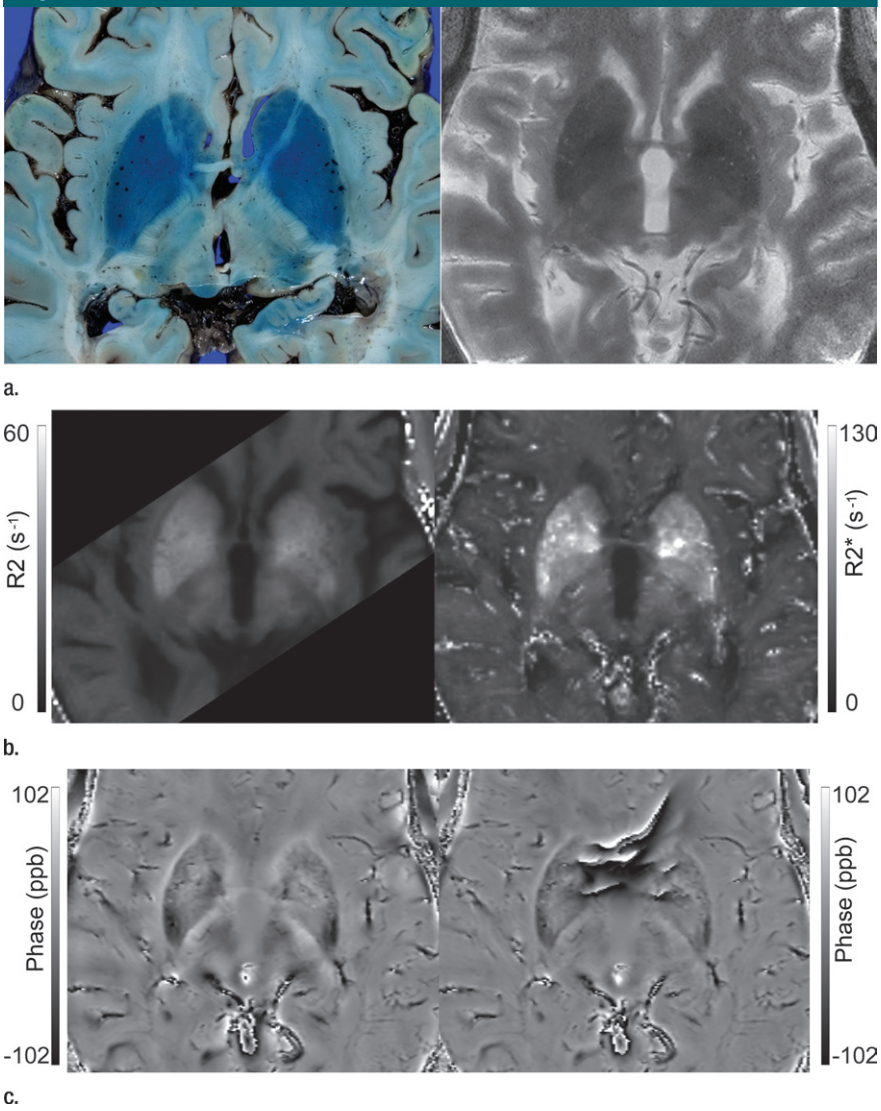

Figure 3: In situ postmortem MR images and photographs of pathology samples from subject 1. **(a)** Corresponding pathology sample (left) stained with Perls iron stain and T2-weighted fast SE MR image (right). **(b)** Corresponding R2 map with six two-dimensional sections (left), which have less coverage than other MR imaging acquisitions, and R2* map (right). **(c)** Corresponding phase images processed with gradient fitting (left) and Hanning (right) methods. Phase wraps were not removed, and contrast within structures was reduced owing to a higher filter width. *ppb* = parts per billion, *s* = seconds.

Subject 2 had 11 regions that contained large chronic plaques, which demonstrated variable staining for iron. Primarily, staining was observed around the periphery (rim) of the plaques, with diffuse patchy staining throughout the lesions. On T2-weighted fast SE MR images, all lesions appeared hyperintense. On phase images, the centers of large lesions appeared primarily isointense or hypointense, while the rims appeared variably hypointense. This did not correspond absolutely to the staining.

Subject 3 had six lesions that demonstrated microscopic evidence of remyelination and were considered to be shadow plaques (Fig 6). Only one lesion was readily identified at macroscopic visual inspection, and all lesions failed to stain for iron. All lesions were hypointense on R2* maps, hyperintense on T2-weighted fast SE MR images, and isointense on phase images.

Discussion

Our study evaluated several MR imaging methods for measuring iron in subcortical gray matter and for detecting iron within and surrounding MS lesions. R2* mapping had the highest correlation with iron staining in subcortical gray matter in each individual postmortem subject. R2 mapping, phase imaging, and T2-weighted fast SE MR appear to have comparable correlations with iron staining, which are moderate to strong. A weaker correlation with phase imaging may have been due to phase contrast dependence on structural shape and not exclusively iron content (39). T2-weighted fast SE MR imaging may have had a weaker correlation because at high field strength, radiofrequency interference produces a spatial variation of flip angles. R2 mapping may have had a weaker correlation because fewer measurements were obtained due to limited section coverage.

Compared with the subjects imaged postmortem, the subject imaged in vivo had substantially higher correlations to iron staining with R2* mapping, R2 mapping, and phase imaging, but a similar correlation with T2-weighted fast SE MR imaging. Anecdotal intersubject comparison was hampered by differences in disease manifestation, blood flow, and oxygenation and, for T2-weighted fast SE MR imaging, by the fact that the transmit radiofrequency field may vary substantially between individuals at high field strength.

Previous studies have evaluated the correlation between MR imaging and quantitative iron measures, although not in MS. A study (21) similar to our own that focused on healthy individuals yielded higher correlations than we obtained for R2* and similar correlations for R2 by using a quantitative spectroscopic method to provide total

Figure 4

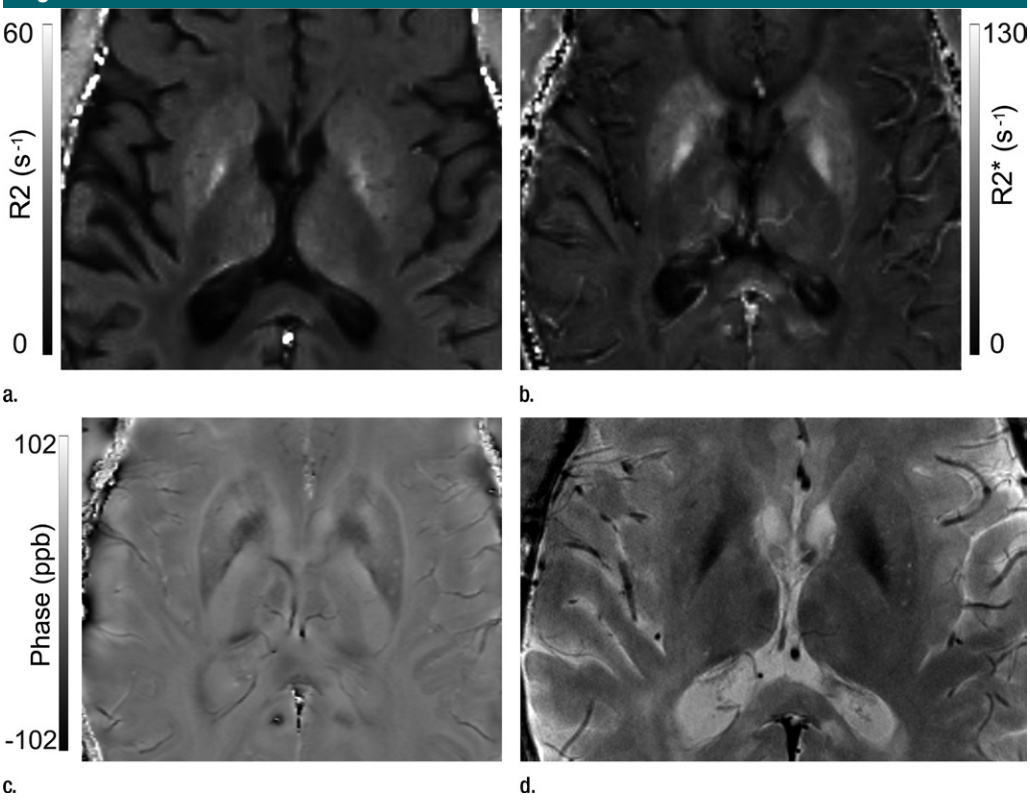

Figure 4: In vivo **(a)** R2, **(b)** R2*, **(c)** phase with gradient background removal, and **(d)** T2-weighted fast SE MR images from subject 4. Note that vessels are less pronounced on **b** and **c,** acquired in vivo versus postmortem (Fig 3). *ppb* = parts per billion, *s* = seconds.

iron in limited sample volumes. In addition, an evaluation (15) of one patient with Alzheimer disease yielded a higher correlation for phase imaging by using x-ray fluorescence mapping for iron. These previous works detected total iron, but the MR imaging measures were mainly sensitive to ferric paramagnetic iron. In our study, Perls iron stain was used to provide a complete slice depiction of ferric iron variation. Although Perls iron staining is generally considered to be qualitative, results of one study (41) demonstrated strong correlations (r = 0.945) between quantitative chemical iron measures and similar optical density measures. In MS, macromolecular mass fraction could be altered as proteins or lipids are degraded or synthesized in response to disease activity, which can alter quantitative MR imaging values (14) without influencing iron staining. Also, prominent features of MS, such as inflammation, neuronal degeneration, demyelination, and cellular swelling, can affect each MR imaging method, but primarily T2-weighted fast SE MR and R2 imaging. These factors limit the ability to compare between cases. Furthermore, correlations may be different because whole-structure ROIs were used, similar to widely used in vivo analysis (16,18,42,43), as opposed to multiple small territories within structures.

In MS lesions in our current study, a single MR imaging method alone could not adequately determine the presence of iron. This is contradictory to results of a previous study (44), which indicated that iron is the dominant source of phase contrast in MS lesions. The pathophysiology of lesions can involve several simultaneous processes (1,22), which can have confounding effects on MR imaging. Myelin loss results in hypointensity on phase and R2* images, while iron accumulation results in hypointensity on phase images and hyperintensity on R2* images. Six nonstaining lesions in subject 1 demonstrated hypointensity on phase images both around the periphery and centrally. Therefore, hypointensity on phase images should not be interpreted as iron in MS lesions (45) since it can also arise from demyelination. R2* maps with lesions displaying a rim of hyperintensity were specific for iron, although not sensitive, and could represent infiltration of inflammatory cells containing iron (22) preceding edema and myelin loss. Subject 3 had shadow plaque MS lesions, which demonstrated no staining and were not visible on phase images, but appeared hypointense on R2* maps. This could indicate that

R2* maps are more sensitive to myelin loss or dysfunction than are phase images when iron is absent.

Advantages of phase imaging include short imaging time, low specific absorption rate, and less sensitivity to water content changes. However, the method of postprocessing can affect the extent of background phase removal and contrast within large deep gray matter structures (40,46,47), where a Hanning filter may be suboptimal in both regards. Furthermore, external field effects from improper background removal or other nearby iron-containing structures could influence measured phase values; therefore, directly adjacent reference phase measures should be obtained. The R2* mapping protocol was also relatively time efficient; however, similar to phase imaging, it can be sensitive to susceptibility differences, such as near air-tissue interfaces or large venous structures. R2 mapping uses SE to refocus the signal in these regions. However, to compensate for a high specific absorption rate, which is problematic at high field strength (48), a limited number of sections and long repetition times were used. Given these constraints, the R2 method used thicker sections and slightly lower in-plane resolution than did the R2* method; thus, spatial resolution differences may have also played a role in the lower correlation with iron. T2-weighted fast SE MR images were acquired at the highest spatial resolution (0.06–0.12 mm^3), which enabled high spatial specificity, but radiofrequency inhomogeneity and additional contrast mechanisms could lead to variable image contrast with this method.

There were several limitations associated with our study. Different parameters were chosen for each MR imaging method, including section thickness, in-plane resolution, and coverage, which could have made direct comparison between methods difficult. The optimal in vivo parameters for each method were used, and these parameters were chosen to achieve appropriate signal-to-noise ratio, image contrast, and imaging time (12). Therefore, the results should have better applicability for in vivo use. An additional limitation is that MR images were acquired in the standard axial plane, while the attending neuropathologist preferred coronal sections in three cases, so MR image reformatting was necessary to achieve correspondence. However, since large ROIs were used around structural borders for quantitative measurements on both pathologic slices and MR images, resolution and original orientation of MR images should not have had a large influence on these measurements because many voxels were averaged. Independent regression analysis was conducted because of variable parameters, including brain duration in formalin and time after death of MR imaging, which precluded a single regression. Therefore, *P* values should be interpreted appropriately, as they have not been corrected for multiple comparisons. In subject 4, additional changes could have taken place over the year between imaging and death, which could affect correlation findings.

Table 3

Perls Iron Staining of Lesions Compared with MR Imaging Intensity

Lesion	Iron Staining	Phase		R2*	
		Center	Rim	Center	Rim
		Subject 1			
1	Complete	Heterogeneous	Hypointense	Heterogeneous	Hyperintense
2	Complete	Hypointense	Isointense	Isointense	Hyperintense
3	Complete	Heterogeneous	Isointense	Hypointense	Hyperintense
4	Complete	Hypointense	Isointense	Isointense	Isointense
5	Complete	Hypointense	Isointense	Hypointense	Isointense
6	None	Hypointense	Isointense	Hypointense	Isointense
7	None	Hypointense	Isointense	Hypointense	Isointense
8	Complete	Hypointense	Isointense	Hypointense	Hyperintense
9	None	Hypointense	Isointense	Hypointense	Isointense
10	None	Hypointense	Hypointense	Hypointense	Isointense
11	Complete	Hypointense	Isointense	Heterogeneous	Isointense
12	None	Hypointense	Hypointense	Hypointense	Isointense
13	None	Hypointense	Isointense	Hypointense	Isointense
		Subject 2			
1	Rim	Isointense	Hypointense	No data	No data
2	Complete	Hypointense	Isointense	No data	No data
3	Rim	Isointense	Isointense	No data	No data
4	Rim	Isointense	Hypointense	No data	No data
5	Rim	Isointense	Hypointense	No data	No data
6	Rim	Isointense	Hypointense	No data	No data
7	Rim	Isointense	Heterogeneous	No data	No data
8	Rim	Isointense	Hypointense	No data	No data
9	Rim	Isointense	Hypointense	No data	No data
10	Rim	Isointense	Hypointense	No data	No data
11	Rim	Isointense	Hypointense	No data	No data
		Subject 3			
1	None	Isointense	Isointense	Hypointense	Isointense
2	None	Isointense	Isointense	Hypointense	Isointense
3	None	Isointense	Isointense	Hypointense	Isointense
4	None	Isointense	Isointense	Hypointense	Isointense
5	None	Isointense	Isointense	Hypointense	Isointense
6	None	Isointense	Isointense	Hypointense	Isointense

Note.—Intensities given are compared with adjacent tissue. Center = MR lesion intensity excluding periphery, Rim = MR intensity of lesion periphery.

Figure 5

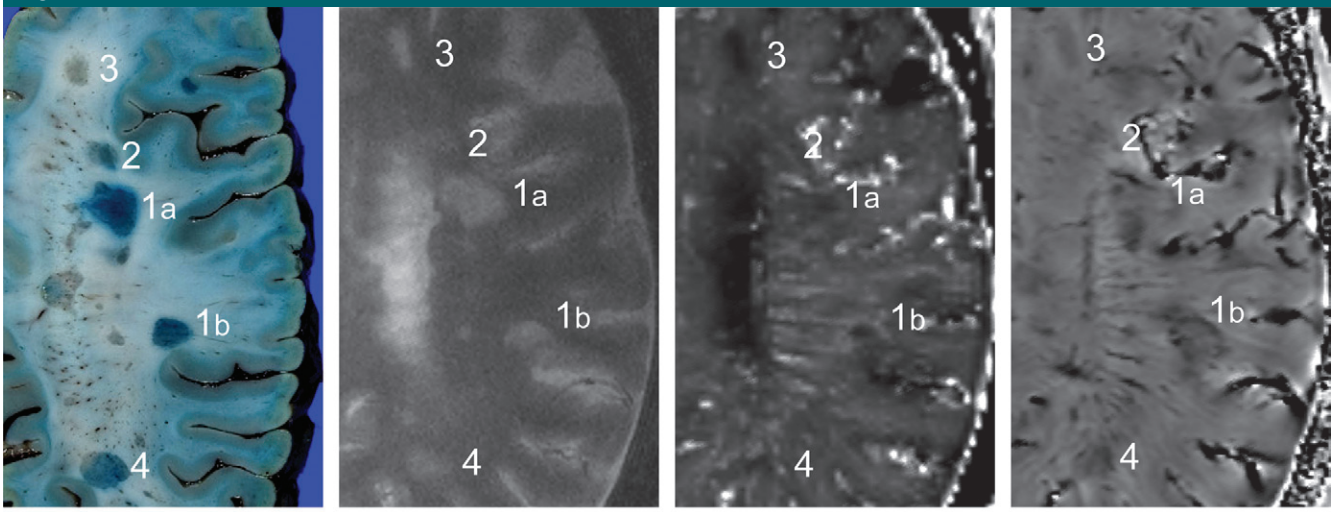

Figure 5: **(a)** Pathology specimen and **(b–d)** in situ postmortem MR images from subject 1. **(a)** Perls iron–stained 8-mm-thick axial cerebral slice superior to the left lateral ventricle with staining *(1a, 1b, 2, 4)* and nonstaining *(3)* lesions. **(b)** T2-weighted fast SE MR image with focal hyperintensities corresponding to both staining and nonstaining lesions. **(c)** R2* map shows two centrally hypointense lesions with hyperintense rims *(1a, 1b)*, an isointense lesion *(2)*, and a hypointense lesion *(4)*, which all correspond to staining lesions. Hypointense lesion *(3)* corresponds to nonstaining lesion. **(d)** Phase image processed with gradient method shows hypointensity in both staining and nonstaining lesions. Partial volume effects are visible from the superior aspect of the left lateral ventricle on **b–d**.

Figure 6

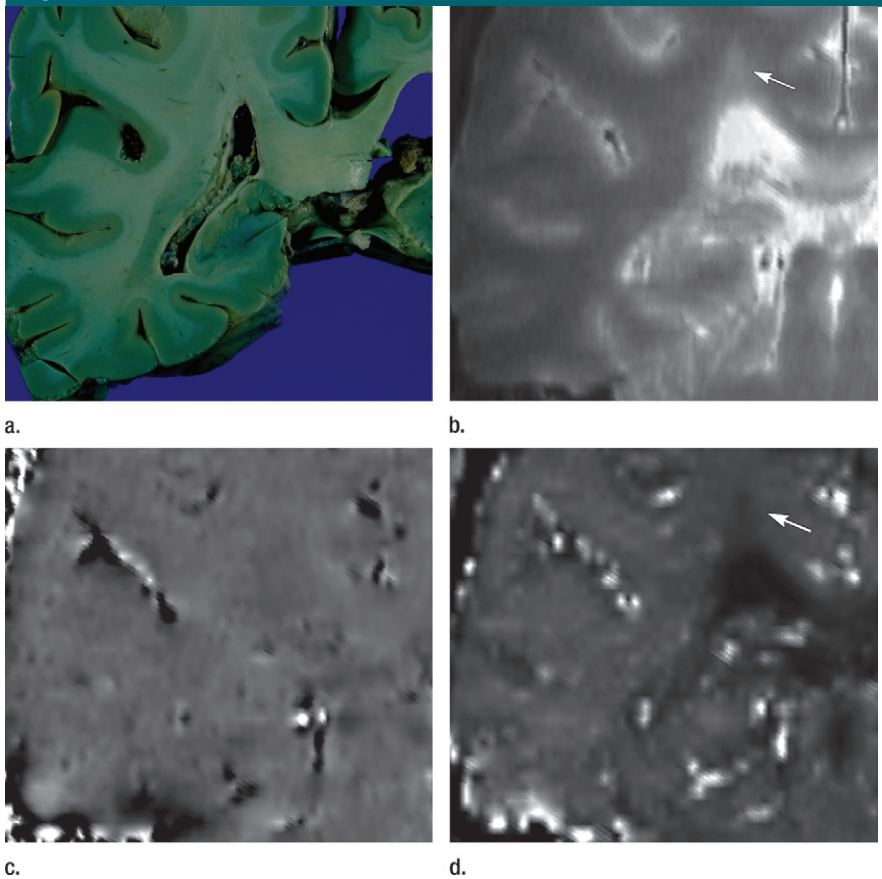

Figure 6: **(a)** Pathology specimen and **(b–d)** in situ postmortem MR images from subject 3 show evidence of shadow plaques as defined by pathologic findings. **(a)** Perls iron–stained 8-mm-thick coronal cerebral slice shows absence of macroscopically identifiable lesions. **(b)** T2-weighted fast SE MR image shows an area of hyperintensity (arrow) corresponding to an MS lesion. **(c)** Phase image shows no visible lesion. **(d)** R2* map shows an area of hypointensity (arrow) corresponding to a lesion.

Furthermore, changes occurring hours after death could also affect iron correlations in subjects 1–3.

In conclusion, subcortical gray matter measurement of transverse relaxation rates (ie, R2 and R2*) and phase imaging, as well as standard T2-weighted fast SE MR imaging, provide good correlation with iron content as measured with Perls iron stain in subject with MS, with R2* having the highest correlation. The relationship between iron and MS lesion appearance on MR images was highly variable owing to the influence of complex pathophysiologic characteristics other than iron on image contrast.

Acknowledgment: We thank Thomas Turner for his assistance with photography of the gross pathologic specimens.

Disclosures of Conflicts of Interest: A.J.W. Financial activities related to the present article: salary grants, CIHR Vanier and AIHS studentship. Financial activities not related to the present article: none to disclose. Other relationships: none to disclose. **R.M.L.** No relevant conflicts of interest to disclose. **A.E.** No relevant conflicts of interest to disclose. **G.B.** Financial activities related to the present article: grants, MS Society of Canada, CIHR. Financial activities not related to the present article: none to disclose. Other relationships: none to disclose. **I.C.** No relevant conflicts of interest to disclose. **J.L.** No relevant conflict of interest to disclose. **L.R.** No relevant conflicts of interest to disclose. **E.S.J.** No relevant conflicts of interest to disclose. **D.J.E.** Financial activities related to the present article: Grant, CIHR. Financial activities not related to the present article: none to disclose. Other relationships: none to disclose. **K.G.W.** No relevant conflicts of interest to disclose. **A.H.W.** Financial activities related to the present article: operating grants, Canadian Institutes of Healt Research, MS Society of Canada. Financial activities not related to the present article: none to disclose. Other relationships: none to disclose.

References

1. Williams R, Buchheit CL, Berman NE, LeVine SM. Pathogenic implications of iron accumulation in multiple sclerosis. J Neurochem 2012;120(1):7–25.
2. Craelius W, Migdal MW, Luessenhop CP, Sugar A, Mihalakis I. Iron deposits surrounding multiple sclerosis plaques. Arch Pathol Lab Med 1982;106(8):397–399.
3. LeVine SM. Iron deposits in multiple sclerosis and Alzheimer's disease brains. Brain Res 1997;760(1-2):298–303.
4. Adams CW. Perivascular iron deposition and other vascular damage in multiple sclerosis. J Neurol Neurosurg Psychiatry 1988; 51(2):260–265.
5. Drayer B, Burger P, Hurwitz B, Dawson D, Cain J. Reduced signal intensity on MR images of thalamus and putamen in multiple sclerosis: increased iron content? AJR Am J Roentgenol 1987;149(2):357–363.
6. Haacke EM, Cheng NY, House MJ, et al. Imaging iron stores in the brain using magnetic resonance imaging. Magn Reson Imaging 2005;23(1):1–25.
7. Schenck JF, Zimmerman EA. High-field magnetic resonance imaging of brain iron: birth of a biomarker? NMR Biomed 2004; 17(7):433–445.
8. Ogg RJ, Langston JW, Haacke EM, Steen RG, Taylor JS. The correlation between phase shifts in gradient-echo MR images and regional brain iron concentration. Magn Reson Imaging 1999;17(8):1141–1148.
9. Shmueli K, de Zwart JA, van Gelderen P, Li TQ, Dodd SJ, Duyn JH. Magnetic susceptibility mapping of brain tissue in vivo using MRI phase data. Magn Reson Med 2009;62(6):1510–1522.
10. Zhang Y, Zabad RK, Wei X, Metz LM, Hill MD, Mitchell JR. Deep grey matter "black T2" on 3 tesla magnetic resonance imaging correlates with disability in multiple sclerosis. Mult Scler 2007;13(7):880–883.
11. Khalil M, Langkammer C, Ropele S, et al. Determinants of brain iron in multiple sclerosis: a quantitative 3T MRI study. Neurology 2011;77(18):1691–1697.
12. Lebel RM, Eissa A, Seres P, Blevins G, Wilman AH. Quantitative high-field imaging of sub-cortical gray matter in multiple sclerosis. Mult Scler 2012;18(4):433–441.
13. Ge Y, Jensen JH, Lu H, et al. Quantitative assessment of iron accumulation in the deep gray matter of multiple sclerosis by magnetic field correlation imaging. AJNR Am J Neuroradiol 2007;28(9):1639–1644.
14. Mitsumori F, Watanabe H, Takaya N. Estimation of brain iron concentration in vivo using a linear relationship between regional iron and apparent transverse relaxation rate of the tissue water at 4.7T. Magn Reson Med 2009;62(5):1326–1330.
15. He X, Yablonskiy DA. Biophysical mechanisms of phase contrast in gradient echo MRI. Proc Natl Acad Sci U S A 2009; 106(32):13558–13563.
16. Wharton S, Bowtell R. Whole-brain susceptibility mapping at high field: a comparison of multiple- and single-orientation methods. Neuroimage 2010;53(2):515–525.
17. Yao B, Li TQ, Gelderen P, Shmueli K, de Zwart JA, Duyn JH. Susceptibility contrast in high field MRI of human brain as a function of tissue iron content. Neuroimage 2009;44(4):1259–1266.
18. Wallis LI, Paley MN, Graham JM, et al. MRI assessment of basal ganglia iron deposition in Parkinson's disease. J Magn Reson Imaging 2008;28(5):1061–1067.
19. Hallgren B, Sourander P. The effect of age on the non-haemin iron in the human brain. J Neurochem 1958;3(1):41–51.
20. Hopp K, Popescu BF, McCrea RP, et al. Brain iron detected by SWI high pass filtered phase calibrated with synchrotron X-ray fluorescence. J Magn Reson Imaging 2010; 31(6):1346–1354.
21. Langkammer C, Krebs N, Goessler W, et al. Quantitative MR imaging of brain iron: a postmortem validation study. Radiology 2010; 257(2):455–462.
22. Bagnato F, Hametner S, Yao B, et al. Tracking iron in multiple sclerosis: a combined imaging and histopathological study at 7 Tesla. Brain 2011;134(Pt 12):3602–3615.
23. Schrag M, McAuley G, Pomakian J, et al. Correlation of hypointensities in susceptibility-weighted images to tissue histology in dementia patients with cerebral amyloid angiopathy: a postmortem MRI study. Acta Neuropathol (Berl) 2010;119(3):291–302.
24. Yao B, Bagnato F, Matsuura E, et al. Chronic multiple sclerosis lesions: characterization with high-field-strength MR imaging. Radiology 2012;262(1):206–215.
25. Dawe RJ, Bennett DA, Schneider JA, Vasireddi SK, Arfanakis K. Postmortem MRI of human brain hemispheres: T2 relaxation times during formaldehyde fixation. Magn Reson Med 2009;61(4):810–818.
26. van Duijn S, Nabuurs RJ, van Rooden S, et al. MRI artifacts in human brain tissue after prolonged formalin storage. Magn Reson Med 2011;65(6):1750–1758.
27. Bischoff K, Lamm C, Erb HN, Hillebrandt JR. The effects of formalin fixation and tissue embedding of bovine liver on copper, iron, and zinc analysis. J Vet Diagn Invest 2008;20(2):220–224.
28. Shepherd TM, Flint JJ, Thelwall PE, et al. Postmortem interval alters the water relaxation and diffusion properties of rat nervous tissue: implications for MRI studies of human autopsy samples. Neuroimage 2009;44(3):820–826.
29. Schrag M, Dickson A, Jiffry A, Kirsch D, Vinters HV, Kirsch W. The effect of formalin fixation on the levels of brain transition metals in archived samples. Biometals 2010;23(6):1123–1127.
30. Lebel RM, Wilman AH. Time-efficient fast spin echo imaging at 4.7 T with low refocusing angles. Magn Reson Med 2009;62(1): 96–105.
31. Lebel RM, Wilman AH. Transverse relaxometry with stimulated echo compensation. Magn Reson Med 2010;64(4):1005–1014.
32. Meguro R, Asano Y, Odagiri S, Li CT, Iwatsuki H, Shoumura K. Nonheme-iron histochemistry for light and electron microscopy: a historical, theoretical and technical review. Arch Histol Cytol 2007;70(1): 1–19.
33. Rasband WS. ImageJ. US National Institutes of Health, Bethesda, Maryland, 1997-2011.
34. Bizzi A, Brooks RA, Brunetti A, et al. Role of iron and ferritin in MR imaging of the

brain: a study in primates at different field strengths. Radiology 1990;177(1):59–65.

35. Vaughan JT, Garwood M, Collins CM, et al. 7T vs. 4T: RF power, homogeneity, and signal-to-noise comparison in head images. Magn Reson Med 2001;46(1):24–30.
36. Baudrexel S, Volz S, Preibisch C, et al. Rapid single-scan T2*-mapping using exponential excitation pulses and image-based correction for linear background gradients. Magn Reson Med 2009;62(1):263–268.
37. Du YPP, Jin ZY, Hu YZ, Tanabe J. Multi-echo acquisition of MR angiography and venography of the brain at 3 Tesla. J Magn Reson Imaging 2009;30(2):449–454.
38. Haacke EM, Xu Y, Cheng YC, Reichenbach JR. Susceptibility weighted imaging (SWI). Magn Reson Med 2004;52(3):612–618.
39. Schäfer A, Wharton S, Gowland P, Bowtell R. Using magnetic field simulation to study susceptibility-related phase contrast in gradient echo MRI. Neuroimage 2009;48(1):126–137.
40. Walsh AJ, Eissa A, Blevins G, Wilman AH. Susceptibility phase imaging with improved image contrast using moving window phase gradient fitting and minimal filtering. J Magn Reson Imaging doi:10.1002/jmri.23768. Published online August 3, 2012.
41. Masuda T, Kasai T, Satodate R. Quantitative measurement of hemosiderin deposition in tissue sections of the liver by image analysis. Anal Quant Cytol Histol 1993;15(6):379–382.
42. Hammond KE, Metcalf M, Carvajal L, et al. Quantitative in vivo magnetic resonance imaging of multiple sclerosis at 7 Tesla with sensitivity to iron. Ann Neurol 2008;64(6):707–713.
43. Pawate S, Wang L, Song Y, Sriram S. Analysis of T2 intensity by magnetic resonance imaging of deep gray matter nuclei in multiple sclerosis patients: effect of immunomodulatory therapies. J Neuroimaging 2012;22(2):137–144.
44. Haacke EM, Makki M, Ge YL, et al. Characterizing iron deposition in multiple sclerosis lesions using susceptibility weighted imaging. J Magn Reson Imaging 2009;29(3):537–544.
45. Hagemeier J, Heininen-Brown M, Poloni GU, et al. Iron deposition in multiple sclerosis lesions measured by susceptibility-weighted imaging filtered phase: a case control study. J Magn Reson Imaging 2012;36(1):73–83.
46. Schweser F, Deistung A, Lehr BW, Reichenbach JR. Quantitative imaging of intrinsic magnetic tissue properties using MRI signal phase: an approach to in vivo brain iron metabolism? Neuroimage 2011;54(4):2789–2807.
47. Liu T, Khalidov I, de Rochefort L, et al. A novel background field removal method for MRI using projection onto dipole fields (PDF). NMR Biomed 2011;24(9):1129–1136.
48. Laule C, Kozlowski P, Leung E, Li DK, Mackay AL, Moore GR. Myelin water imaging of multiple sclerosis at 7 T: correlations with histopathology. Neuroimage 2008;40(4):1575–1580.